Article

TSC-1 Optical Payload Hyperspectral Imager Preliminary Design and Performance Estimation

Weerapot Wanajaroen [1,2,*] **, Christophe Buisset** [1]**, Thierry Lépine** [3,4]**, Pearachad Chartsiriwattana** [1]**,
Merisa Kosiyakul** [1]**, Apirat Prasit** [1]**, Phongsatorn Saisutjarit** [5]**, Suwicha Wannawichian** [2]**, Wiphu Rujopakarn** [1]**,
Saran Poshyachinda** [1] **and Boonrucksar Soonthornthum** [1]

[1] National Astronomical Research Institute of Thailand (Public Organization), 260 Moo 4, T. Donkaew,
A. Maerim, Chiang Mai 50180, Thailand
[2] Department of Physics and Materials Science, Faculty of Science, Chiang Mai University,
Chiang Mai 50200, Thailand
[3] Institut d'Optique Graduate School, 18 Rue Benoit Lauras, 42000 Saint-Etienne, France
[4] Laboratoire Hubert Curien, Université de Lyon, CNRS, 18 Rue Benoît Lauras F, 42000 Saint-Etienne, France
[5] Department of Mechanical and Aerospace Engineering, Faculty of Engineering, King Mongkut's University of
Technology North Bangkok, Wongsawang Bang Sue, Bangkok 10800, Thailand
* Correspondence: weerapot@narit.or.th; Tel.: +66-8-5549-6026

Abstract: The Thai Space Consortium aims at building capacities in space technologies and industries with the objective to develop satellites in Thailand. In this framework, the first Earth Observation satellite that will be developed by this consortium is called TSC-1. This satellite comprises a hyperspectral imager orbiting in a Sun-Synchronous Low-Earth Orbit at the altitude equal to 630 km. The optical payload is specified to provide data cubes with a Ground Sample Distance equal to 30 m, a swath equal to 30 km, a spectral resolution equal to 10 nm over the spectral domain from 400 nm to 1000 nm with a Signal-to-Noise Ratio (SNR) higher than 100. Firstly, we present the trade-off performed to select the design of the Front Telescope and the Spectrometer. Secondly, we describe the payload design and present the image quality, Modulation Transfer Function and distortion. Next, we establish the tolerance budget to estimate the performance of the optical system including manufacturing errors, assembly errors and stability of the mechanical structure. After that, we calculate the instrument's spatial and spectral response functions and the contamination of the adjacent pixels due to the straylight. Finally, we estimate radiometric performance in both nadir pointing mode and forward motion compensation mode.

Keywords: hyperspectral imaging; remote sensing; satellite payload

1. Introduction

1.1. TSC-1 Mission, Context and Impact on Technical Choices

Thai Space Consortium (TSC) comprises twelve Thai national organizations led by the National Astronomical Research Institute of Thailand (NARIT), the Geo-Informatics and Space Technology Development Agency (GISTDA), the Synchrotron Light Research Institute (SLRI) and the King Mongkut's University of Technology North Bangkok (KMUTB). The long-term objective of the consortium is to elevate the capacities to design, develop and test space optical payloads in Thailand. In this context, the objective of the TSC-1 space mission is to send into space a satellite made of one platform, one optical payload dedicated to Earth observations, and one space weather payload. The optical payload would consist of hyperspectral imager pledge data cubes in the visible band. The Ground Sample Distance (GSD) is equal to 30 m, while the spectral sampling is equal to 5 nm/pixel. Therefore, the final spectral resolution is equal to 10 nm when the entrance slit of the spectrometer covers two rows of pixels.

The NARIT Center for Optics and Photonics (COP) is responsible for the development of the TSC-1 optical payload. NARIT COP has a proven experience in the development of the optical system for astronomical applications with wide-field cameras and low- and high-resolution spectrographs successfully commissioned on the 2.4 m Thai National Telescope (TNT) [1–5]. A space-based hyperspectral imager thus constitutes the next step in the development of optical systems at NARIT COP.

TSC-1 Earth Observation optical payload constitutes the first optical space system for a small satellite developed by Thailand. We thus decided to restrict some technical choices to guarantee the payload's feasibility. We decided to select only spherical or aspherical optical surfaces and to put priority on using on-axis optical surfaces. We thus decided to avoid using freeform optics for this first optical payload. We want to develop one payload able to perform coastal, ocean and land observation similar to Sentinel-3 OLCI [6] that focuses mainly on Thailand. With this starting point, we will have no constraints on the revisit time and temporal average. Instead, we can have a better spatial resolution and an SNR equal to 100. This targeted application requests a spectral domain from 400 nm to 1000 nm compatible with COSTs CMOS spectral range. The volume/mass of the instrument is also compatible with the programmatic constraints. The specifications of the TSC-1 hyperspectral imager are presented in the next section.

The Sentinel-3 Earth observation satellite made by ESA was launched in 2016. One of the payloads in Sentinel-3 is a hyperspectral imager named Ocean and Land Colour Instrument (OLCI). The objectives of Sentinel-3 OLCI are to provide useful data to support ocean missions, land missions, atmospheric properties, river and lake level monitoring, sea surface temperature, ocean colour and wind and ocean waves [6]. The OLCI swath width is equal to 1270 km. The spatial sampling is equal to 300 m. It provides 21 spectral bands over the 400–1020 nm spectral range. The spectral resolution varies between 7.5 nm and 20 nm. There are special bands which are the 759–763 nm band that has the finest resolution at 3.75 nm for oxygen absorption band and aerosol correction and the 1000–1040 nm band that has the lowest resolution at 40 nm. The SNR of OLCI varies between 300 and 2000 where the highest SNR is obtained in the shortest wavelength. The lowest SNR is obtained in the longest wavelength. The mass of OLCI is equal to 153 kg. The size is equal to 1.3 m^3. TSC-1 hyperspectral imager is capable of finer spatial resolution in a smaller form factor and lower mass. TSC-1 payload weight and volume are less than 30 kg and $700 \times 700 \times 300$ mm^3 respectively. In terms of spectral resolution, the TSC-1 hyperspectral imager performance is comparable to the Sentinel-3 OLCI.

On the other hand, the TSC-1 hyperspectral imager's specifications are close to the EnMAP hyperspectral imager. EnMAP swath width and spatial resolution are equal to 30 km and 30 m respectively [7] as for the TSC-1 optical payload. The aperture number is equal to 3. EnMAP spectral resolution is equal to 6.5 nm over the VIS spectral band. The SNR is equal to 500 at λ = 495 nm. However, EnMAP hyperspectral imagers are quite complex using a double-pass Offner configuration with the implementation of two curved prisms. In addition, the EnMAP VIS spectrometer alone already occupies a lot of space which is not compatible with our volume requirements.

We thus consider that the main interest of this work is to describe a space hyperspectral imager dedicated to Earth Observation that represents the best compromise between the performance and the technical capabilities of an institute in a developing country, which has successfully developed a few optical instruments for astronomical observations. However, the unknown factors of the space environment are our concerns. The extreme temperature of the satellite, while the satellite is exposed to sunlight, must be taken into account. There will be at least one side facing deep space and another side always facing the Sun. This causes a huge temperature difference between these two sides of the satellite. It directly relates to the mechanical structure of the gravity-released expansions of the mounts, and the optics as well as the optical surface deformation due to the thermal expansion and gravity-released effect. Therefore, we must aim at the best optical performance to keep some margins for these unknown factors. We also started doing the preliminary mechanical

and thermal analysis to ensure that the system will survive in the space environment. The results from the mechanical analysis will be taken into account in the optical system tolerance analysis. In addition, the satellite will be exposed to the environment that causes the straylight in the optical payload. The straylight degrades the quality of the hyperspectral image. Therefore, we have designed a baffling system to protect the optical system from unwanted light. However, we would like to keep the optical design simple but well-working. This must be a good balance between performance and technical capabilities. We believe that the description of the methods we used to select the design and develop the tools to estimate the performance will represent a source of interest for similar institutes and research centers in emerging countries. In parallel with the current technical activities, the TSC is evaluating the scientists' needs for data processing. Thus, the objective is to identify the best processing method to maximize the scientific output of the mission dedicated to the observation and monitoring of coastal, ocean, land, river level, and atmospheric properties.

1.2. TSC-1 Payload Scientific Objectives and Specifications

The TSC-1 optical payload specifications are presented in Table 1. This payload will be located on a Sun-Synchronous orbit at the altitude equal to 630 km and will provide data cubes over the spectral domain from 400 nm to 1000 nm. The specified GSD and Field Of View (FOV) are equal to 30 m and 30 km respectively. We selected a detector CMOSIS CMV4000 2048 × 2048 pixels whose 5.5 μm pixel is widely used in the new generation of hyperspectral imagers in small satellites. We will use the readout software to combine the signal from a group of 2 × 2 pixels into one data, as a binning technique. The binning technique allows the increase of the SNR because the effective pixel is bigger, hence more signal is integrated. It is important to mention that we will call this group of 2 × 2 pixels (super pixel) a pixel afterward. The detector format to cover the full FOV and the full spectral domain is equal to 1000 × 120 pixels. The other pixels that do not collect any scientific signal will be cropped out later. The Modulation Transfer Function (MTF) [8] is specified to be higher than 0.3 at the Nyquist frequency fn = 45 cycles/mm. The spectral response Full Width at Half Maximum (FWHM) is specified to be equal to 10 nm. The payload will provide a Signal to Noise Ratio (SNR) higher than 150 for an incident radiance $L = 70$ W/m^2·sr·μm over the full specified spectral domain. The mass of the payload is specified to be lower than 30 kg for a maximum volume equal to 700 mm × 700 mm × 300 mm.

Table 1. TSC-1 Optical Payload specifications.

Parameter	Specification
Instrument concept	Visible Hyperspectral Imager
Orbit	Low Earth, Sun Synchronous Orbit
Altitude	630 km
Spel domain	[400 nm, 1000 nm]
Ground Sampling Distance, FOV	30 m, 30 km
Modulation Transfer Function	MTF > 0.3 at Nyquist Frequency
Spectral Response FWHM	10 nm
Signal to Noise Ratio	SNR > 100 at $L = 70$ W/m^2/sr/μm
Detector	CMOSIS CMV4000
Pixel size and detector format	11 μm, 1000 × 120
Mass	<30 kg
Dimension	<700 mm × 700 mm × 300 mm

2. Front Telescope Design Trade-Off

2.1. Optical Design and Theoretical Performance

We have designed and estimated the performance of two Front Telescopes by using Zemax OpticStudio [9]. One telescope has a real aperture stop floating in the air which eases the implementation of the diaphragm to reduce the straylight. The other telescope

has an aperture stop located on one of the optical surfaces. We have compared the design and performance of two Front Telescope designs called FT1 and FT2 respectively. FT1 (Figure 1, left panel) is made of two mirrors, FT1-M1 and FT1-M2. FT1-M1 is an off-axis mirror of a diameter equal to 100 mm and decenter equal to 65 mm. The radius of curvature is equal to 471 mm and the conic constant is equal to +2.2. FT1-M2 is a centered mirror of diameter equal to 250 mm, the radius of curvature and conic constant equal to 680 mm and +0.2 respectively. FT1-M2 constitutes both the Aperture Stop (AS) and the exit pupil. Consequently, FT1 is not telecentric, in which the exit pupil is located at a distance approximately equal to 650 mm from the image plane.
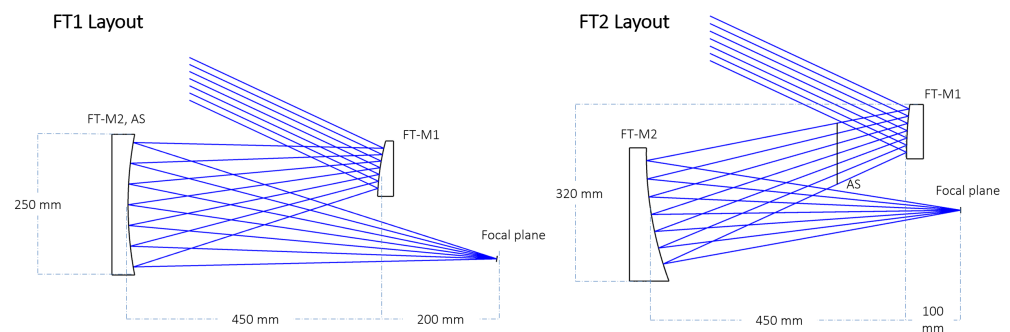

Figure 1. FT1 (**left**-panel) and FT2 (**right**-panel) optical layouts.

The optical design layout of the second solution, FT2, is presented in Figure 1-right-panel. The incident beam is reflected by FT2-M1 toward the Aperture Stop (AS), FT2-M2 and the focal plane. The AS is real and located between FT2-M1 and FT2-M2. The AS diameter is equal to 105 mm, where the system is telecentric. FT2-M1 is a convex off-axis mirror of diameter equal to 100 mm and decenter equal to 38 mm. FT2-M2 is a concave off-axis mirror of diameter equal to 230 mm and decenter equal to 105 mm. The FT2-M1 (respectively FT2-M2) radius of curvature is equal to 670 mm (respectively 540 mm) and the conic constant is equal to +6.2 (respectively +0.2). The optical parameters of FT-1 and FT-2 are summarized in Table 2.

Table 2. FT1 and FT2 optical parameters.

	Parameter	FT1	FT2
M1	Radius	470 mm	670 mm
	Diameter	100 mm	100 mm
	Conic constant	+2	+6.2
	Off-axis decenter	65 mm	38 mm
M2	Radius	680 mm	640 mm
	Diameter	255 mm	230 mm
	Conic constant	+0.2	+0.2
	Off-axis decenter	-	105 mm

We are interested in only the optical performance of the specified FOV and specified spectral band. The spot diagrams of FT1 and FT2 are represented in Figure 2. We notice that in the theoretical case, the RMS spot radius is smaller than 3 μm. That is comparable to the airy radius equal to 2.6 μm. We thus conclude that the image qualities of these two designs are, in theory, close to the diffraction over the specified FOV.
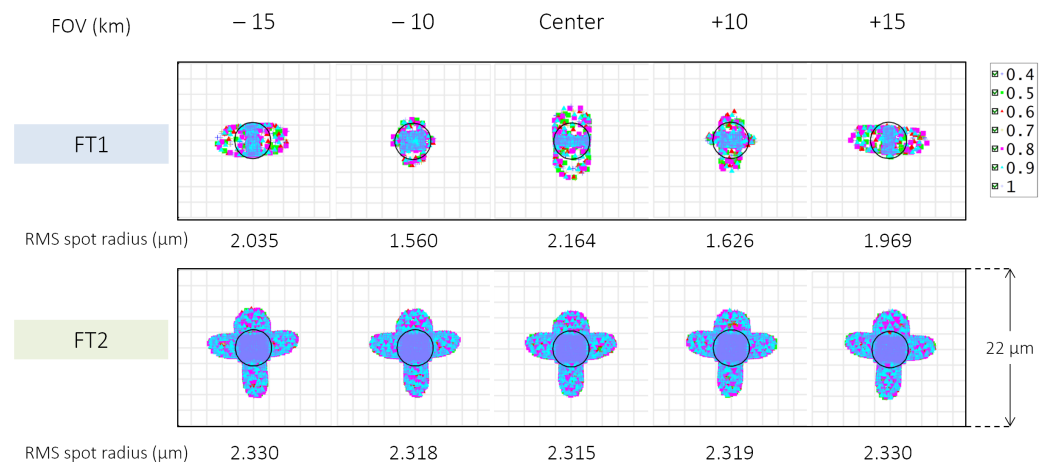
FOV (km)	− 15	− 10	Center	+10	+15

FT1

0.4
0.5
0.6
0.7
0.8
0.9
1

RMS spot radius (µm)	2.035	1.560	2.164	1.626	1.969

FT2

22 µm

RMS spot radius (µm)	2.330	2.318	2.315	2.319	2.330

Figure 2. FT1 and FT2 spot diagrams are presented on top and bottom panels, respectively.

We notice a slight variation of the spot image over the FOV for FT1, while the image quality is remarkably stable for FT2. However, these results correspond to the theoretical case only and we can expect that the misalignment induced by the alignment, launch and thermo-elastic effects will introduce in-field variation of the spot image for both systems. We conclude that the theoretical image quality of both telescopes is similar, with a comparable spot radius, which is much smaller than the pixel size.

We calculated the distortion of both FT designs. We found that the distortion of FT1 (respectively FT2) is equal to 218% of the pixel (respectively 255%). The consequence of this distortion is the need for a curved slit as represented in Figure 3. The length of the slit must cover the specified FOV at the focal plane of the front telescope, while the image of the slit width must cover two pixels on the spectrometer image plane. In the case of TSC-1, the slit length (respectively width) is equal to 11 mm (respectively 22 µm). The deviation at the edge of the slit is equal to 24 µm for FT1 and equal to 28 µm for FT2. It is important to mention that the curved slit is always included in all simulations we have done.
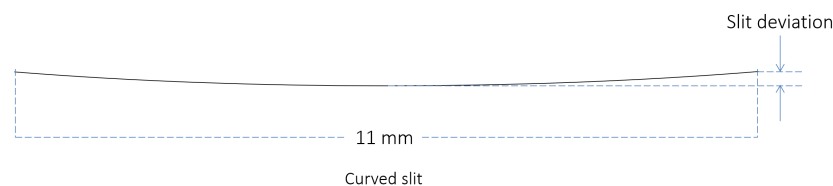
Slit deviation

11 mm

Curved slit

Figure 3. Curved slit drawing. The Slit length is equal to 11 mm and the width is equal to 22 µm. The slit deviation is due to FT distortion and is equal to 24 µm for FT1 and 28 µm for FT2.

2.2. Sensitivity Matrix

The sensitivity of the optical system is estimated to realize the sensitive component to the misalignment errors. This leads us to put on the mechanical limit of each optical component to restrict the error of the optical component mounting mechanism.

We established the sensitivity matrix of FT1 and FT2 by calculating the variations ΔR of the spot radius for a given decenter and tip/tilt errors of each mirror. The decenter is equal to 0.1 mm in every direction for each mirror. The FT-M1 (respectively FT-M2) tip/tilt errors are equal to ±0.1 degree (respectively 0.05 degree). These angles correspond to a displacement of the mirror surface equal to 0.1 mm at the edge. It is important to mention that the error is applied to the optical system one at a time to precisely estimate the impact of each individual error on the optical performance.

Table 3 presents the enlargement of the RMS spot radius at the FOV center and a wavelength equal to 700 nm. In the perfect case (no misalignment), the spot radius is equal to 2.2 µm. We notice that the most sensitive parameter for both telescope designs is the

tip/tilt of both mirrors (FT-M1 and FT-M2) which introduces a variation ΔR in the range of 6.7–11.2 μm. Even though FT2 is less sensitive, the variation ΔR is still significant when compared to the pixel size of 11 μm.

Table 3. Front Telescope sensitivity matrix represents in term of ΔR RMS spot radius calculated at FOV center and λ = 700 nm.

Component	Parameter	Error	FT1 Max ΔR (μm RMS)	FT2 Max ΔR (μm RMS)
FT-M1	Decenter X	±0.1 mm	1.8	0.9
	Decenter Y	±0.1 mm	2.2	2.3
	Tilt X	±0.1 degrees	11.2	9.0
	Tilt Y	±0.1 degrees	10.3	9.1
FT-M2	Decenter X	±0.1 mm	1.8	0.9
	Decenter Y	±0.1 mm	2.6	2.3
	Tilt X	±0.05 degrees	11	7.2
	Tilt Y	±0.05 degrees	9.9	6.7

2.3. Front Telescope Design Selection

The main conclusions of the trade-off between FT1 and FT2 are presented in Table 4. We decided to select the FT1 design for the reasons explained hereafter.

Table 4. TSC-1 Front Telescope Assembly trade-off summary.

System	Advantage	Drawback
FT1	Physical and accessible Aperture Stop located on FT-M2 >Good control of straylight. One large centered concave mirror with a small deviation from reference sphere >Easy to manufacture and control. Only one small convex off-axis mirror with reasonable conic constant >Reasonable effort to manufacture and align.	Non-telecentric system >Not fully compatible with a telecentric spectrometer Smile distortion >Implies curved slit at spectrometer entrance
FT2	Accessible Aperture Stop >Ease the baffling system design Telecentric system >Compatible with the telecentric spectrometer	Two off-axis aspherical mirrors and high conic constant for FT1- M1 >Difficult to manufacture and align, increase overall cost and risk. Higher volume than FT-1 to accommodate physical AS between M1 and M2 >Increases payload volume and mass. Smile distortion >Implies curved slit at spectrometer entrance

The first advantage of FT1 is the possibility to accommodate some physical stops that ease the control of the straylight. The second advantage is that FT1-M2 is a centered mirror that is easy to fabricate and control. Furthermore, this telescope comprises one small off-axis mirror of conic constant equal to +2, which is considered manufacturable with a reasonable cost. The optical layout is included in a volume equal to $250 \times 250 \times 650$ mm^3, which is identified as the most compact design solution. We have been able to reach obvious gains in payload overall volume and mass. The FT1 main drawback is that the system is not telecentric. Indeed, the exit pupil is located at a distance equal to 650 mm from the slit plane.

The advantages of FT2 are the accessibility of physical stop and the ease to control of straylight. The FT2 theoretical image quality and the sensitivity to the misalignment are comparable to FT1. The main drawback is that FT2 is made of two off-axis aspherical surfaces. The conic constant of FT2-M1 is particularly high and equal to +6. It means that the deviation from the reference sphere is high and that this mirror will be particularly difficult and expensive to manufacture. We also expect that the alignment of FT2 will be particularly complex and too risky in terms of planning and cost for the first space optical system developed in Thailand.

3. Spectrometer Design Trade-Off

Previously, we had been working on exploring spectrometer designs [10] to estimate the capability of those designs and configurations. We were exploring four spectrometer configurations which are prism-based, Offner, three-mirror-anastigmat, and Dyson spectrometers. The spectrometers that are presented in the survey are the ones that show an interesting design and provide good performance out of the thirty systems that we had been reviewing. Finally, we selected two spectrometer configurations which are Dyson and Offner. These two configurations will be designed, estimated performance, and compared to be the chosen one that is suitable for our mission requirements including feasibility to manufacture, image quality, volume, mass, sensitivity, and cost.

3.1. Dyson Spectrometer Design

The conventional Dyson spectrometer [11] comprises one Dyson lens and one concave grating as represented in Figure 4. In theory, the object plane and the image plane of the conventional Dyson spectrometer are located on the back face of the Dyson lens. The system is telecentric and the magnification is equal to -1. The relation between the radius of curvature R_L and R_M of the Dyson lens (optical index of refraction n) and of the reflective grating is $R_L = (n-1) \cdot R_M / n$.
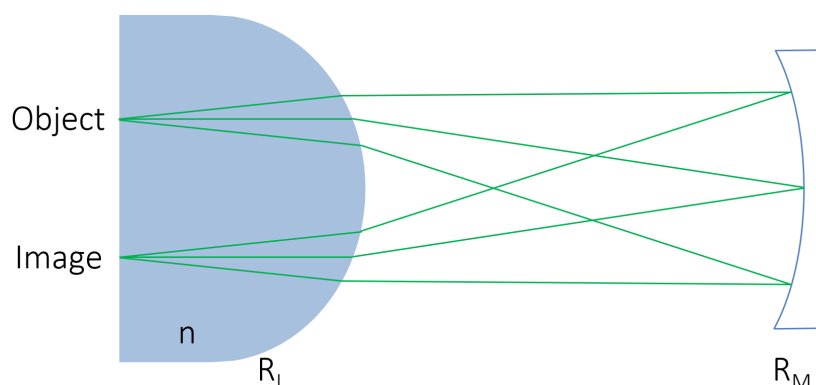

Figure 4. Conventional Dyson spectrometer layout.

In practice, we need a minimum distance to be able to accommodate the detector. The separation between the object/the image planes and the Dyson lens introduces spherical aberration [12]. At least one aspherical surface is required to correct this aberration.

This aspherical surface can be located either on the Dyson lens, the grating or eventually on an additional lens located between the Dyson lens and the grating.

Our design was inspired by the Compact Wide-swath Imaging Spectrometer CWIS [13,14]. The CWIS Dyson spectrometer comprises one concave grating and one cemented doublet. CWIS spectrometer is specified to deliver spectrum over the spectral domain 0.38–2.5 μm and over a field of view equal to 52 degrees. We understood that the additional lens was required to extend the spectral band or the FOV with respect to the classical Dyson design. CWIS doublet is made of Fused Silica and CaF2 material. It is important to mention that CaF2 material is very fragile and difficult to handle. We thus preferred for TSC-1 the combination of Fused Silica and K10.

The optical design layout of the Dyson spectrometer optimized for TSC-1 is presented in Figure 5 left-panel. The beam provided by the FT is incident on the entrance slit that transmits the beam toward the Dyson lens and the concave grating. The light is diffracted by the grating and reflected back to the Dyson lens and focused onto the detector.
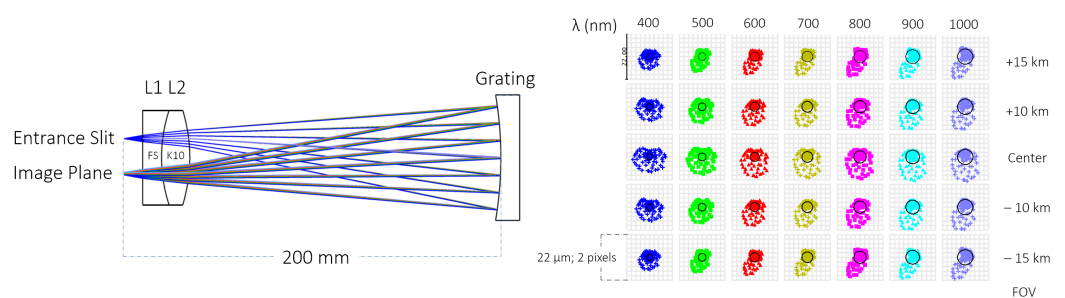

Figure 5. Dyson spectrometer optical layout. The slit is perpendicular to the figure (**left**-panel) and spot diagram (**right**-panel).

The Dyson lens is a cemented doublet made of two lenses, called L1 and L2 respectively. The distance between the Dyson lens and the plane that comprises the slit and the detector is equal to 10 mm. L1 is a plano-concave lens made of fused silica. L1 thickness is equal to 10 mm and the diameter is equal to 50 mm. The radius of curvature of the curved surface is equal to 80 mm. L2 is a bi-convex lens made of K10 of diameter equal to 50 mm and thickness equal to 15 mm. The radius of curvature of the convex surfaces is equal to 80 mm. The first surface of L2 is spherical and the second surface is aspherical of conic constant equal to −2.6. The radius of curvature of the concave grating is equal to −200 mm. The diameter is equal to 66 mm, and the line density is equal to 13 lines/mm.

The spot diagrams are presented in Figure 5 right-panel. The spot image is nearly homogenous over both the specified FOV and spectral domain. The maximum spot radius is at the FOV center for the 1000 nm wavelength, which is equal to 3.9 μm.

We estimated the smile and keystone distortions of the Dyson spectrometer, where the smile distortion is caused by the dispersion variation with respect to the field of view, and the keystone is caused by the magnification variation with respect to the wavelength [11]. The in-field variation of the smile and keystone distortions are represented in Figure 6. We noticed that smile distortion does not only vary with respect to the field of view only but with respect to the wavelength as well. The maximum smile distortion is equal to 3.7 μm at the edge of the FOV of λ = 1000 nm which is equal to 34% of the pixel size. The maximum keystone distortion is equal to 12 μm at the edge of the FOV of λ = 1000 nm which is larger than a pixel of 11 μm.

In comparison with the CWIS [13,14], our Dyson spectrometer provides a smaller spot size which is approximately two-thirds of the CWIS RMS spot radius. However, TSC-1 FOV is much smaller than CWIS. In addition, CWIS distortions are lower than 1 μm. We would like to mention again that the CaF2 material that is used in CWIS provides remarkable optical performance. However, we had an experience with this material once and found that it is very fragile. Therefore, we rather chose another glass combination to avoid having an issue with this material later.
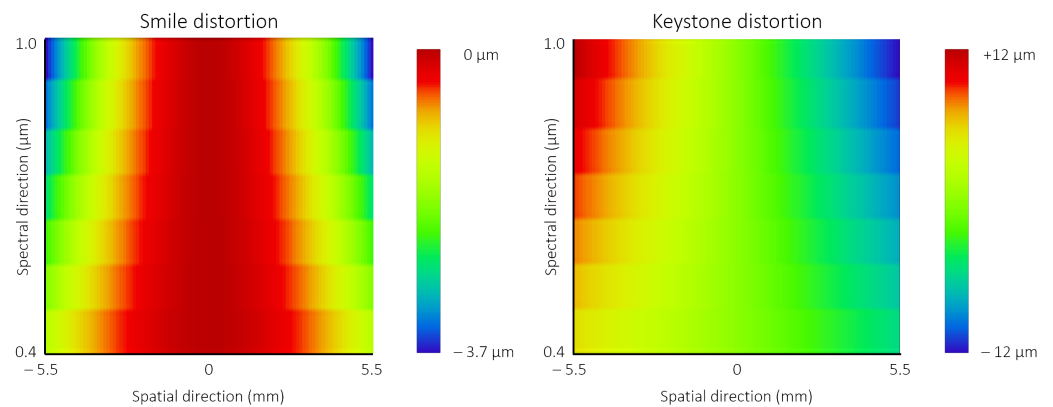
Figure 6. Dyson spectrometer Smile (**left**-panel) and Keystone (**right**-panel) variations.

We established the sensitivity matrix of the Dyson spectrometer by decentering and tilting each optical component and by calculating the spot radius enlargement. Firstly, a misalignment of 0.1 mm is applied for decentering the Dyson lens and the grating. Secondly, we introduced a tip/tilt equal to 0.23 degrees for the Dyson lens and 0.17 degrees for the grating around both the X and Y axes. These tilt values correspond to a displacement of 0.1 mm at the edge of the optical component.

The sensitivity matrix of the Dyson spectrometer considered at the FOV center and $\lambda = 700$ nm is presented in Table 5. We notice that the maximum RMS spot size variation is induced by the grating tilt around X that induces enlargement of the spot radius equal to 1.8 μm. That corresponds to approximately 16% of the pixel size and thus shows that the Dyson spectrometer is robust to the misalignments.

Table 5. TSC-1 Dyson spectrometer sensitivity matrix at FOV center and $\lambda = 700$ nm.

Component	Parameter	Error	Max ΔR (μm RMS)
Dyson lens	Decenter X	±0.1 mm	0.3
	Decenter Y	±0.1 mm	0.4
	Tilt X	±0.23 degrees	0.8
	Tilt Y	±0.23 degrees	0.3
Grating	Decenter X	±0.1 mm	0.3
	Decenter Y	±0.1 mm	0.6
	Tilt X	±0.17 degrees	1.8
	Tilt Y	±0.17 degrees	0.2

3.2. Offner Spectrometer Design

The conventional Offner spectrometer [11] is made of one concave mirror and one convex reflective grating as represented in Figure 7. The mirror and the grating have a common center of curvature called "C". This center of curvature is located on the plane that comprises both the object and the image. On this plane, C is located halfway between the object and the image. The Offner spectrometer is telecentric by design, while the transverse magnification is equal to 1. In the conventional Offner spectrometer: $d_1 = d_2 = R_1/2 = R_2$, where d_1 (respectively d_2) are the distances between the apex of the concave mirror (respectively the apex of the convex grating) and C. R_1 (respectively R_2) is the radius of curvature of the concave mirror (respectively the radius of curvature of the convex grating).

The optical design layout of our Offner spectrometer is represented in Figure 8 left-panel. The beam provided by the telescope is incident on the entrance slit, which transmits the beam toward the mirror SP-M1 and the convex grating (Aperture Stop). The beam diffracted by the grating is reflected by SP-M1 and focused onto the detector. SP-M1 is a concave spherical mirror with a radius of curvature and diameter equal to 102 mm and 100 mm respectively. The grating is engraved on a convex spherical mirror with a radius of

curvature and diameter equal to 51 mm and 25 mm respectively. This grating comprises 40 lines/mm.
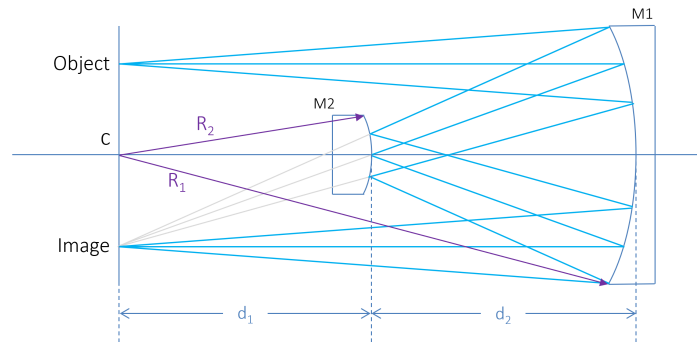

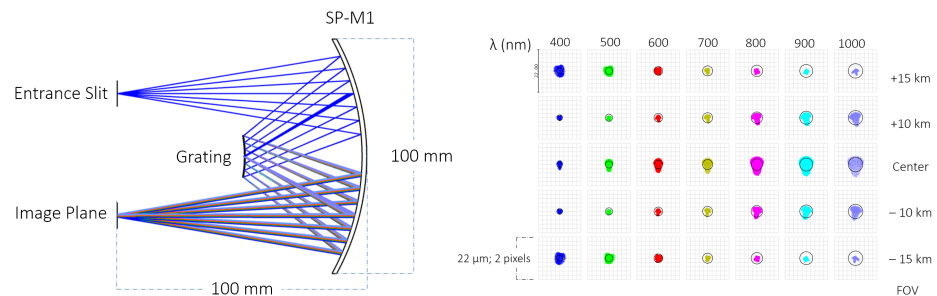**Figure 7.** Conventional Offner spectrometer layout.

Figure 8. Offner spectrometer optical layout. The slit is perpendicular to the figure (**left-panel**) and spot diagram (**right-panel**).

The spot diagram represented in Figure 8 right-panel shows that the spectrometer is diffraction limited over the specified FOV and the spectral range from 500 nm to 1000 nm. While the spectral range from 400 nm to 500 nm is not too far from the diffraction limit. We calculated that the maximum smile distortion (respectively keystone distortion) is equal to 0.1 μm (respectively 0.8 μm) which corresponds to approximately <1% of the pixel size (respectively <8%). The smile and keystone distortion variations are presented in Figure 9.
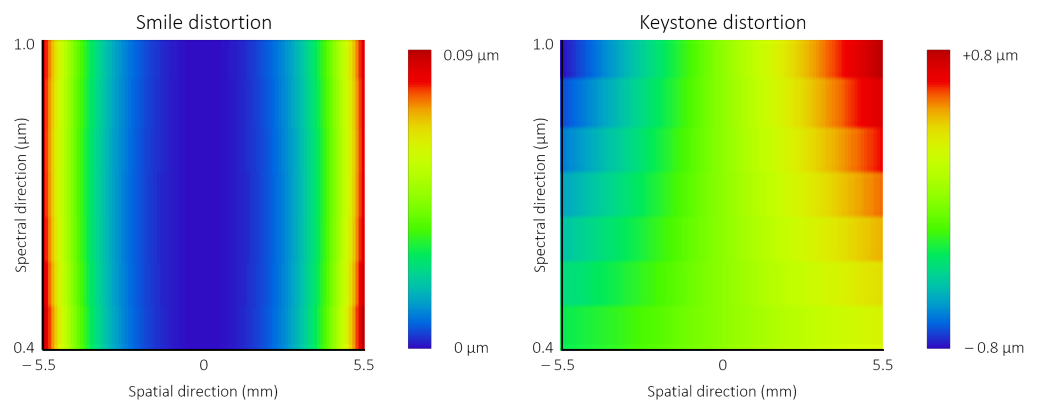

Figure 9. Offner spectrometer Smile (**left**-panel) and Keystone (**right**-panel) variations.

In comparison with Offner–Chrisp compact freeform Mangin design [15] which comprises two freeform mirrors and one convex freeform grating, the freeform Offner provides diffraction-limited performance over the same specified FOV and spectral range with much smaller volume at 100 cm^3. This is 10 times smaller than our spherical Offner design. However, this confirms that our design can reach the diffraction limit without using any aspherical or freeform optics.

The Offner spectrometer sensitivity matrix is presented in Table 6. We decentered both SP-1 and the grating by 0.1 mm. We also injected a tilt in both X and Y directions equal to 0.1 degrees for SP-M1 and equal to 0.6 degrees for the grating. These tilt values correspond to a displacement of 0.1 mm at the edge of the optical component. The maximum variation of the spot radius which is induced by the grating tilt around X is equal to 4 μm RMS which corresponds to 36% of the pixel size. We conclude that the Offner spectrometer is robust to the misalignment but slightly more sensitive than the Dyson spectrometer.

Table 6. TSC-1 Offner Spectrometer sensitivity matrix at FOV center and λ = 700 nm.

Component	Parameter	Error	Max ΔR (μm RMS)
SP-M1	Decenter X	±0.1 mm	0.2
	Decenter Y	±0.1 mm	1.1
	Tilt X	±0.1 degrees	2.3
	Tilt Y	±0.1 degrees	0.1
Grating	Decenter X	±0.1 mm	0.2
	Decenter Y	±0.1 mm	0.7
	Tilt X	±0.6 degrees	3.7
	Tilt Y	±0.6 degrees	0.7

3.3. Trade Off and Design Selection

The trade-off between the two spectrometers is summarized in Table 7. The main advantage of the Dyson spectrometer is the shape of the grating, which is concave. Indeed, a concave grating is significantly easier to manufacture than a convex grating. Unfortunately, the Dyson spectrometer presents several disadvantages. Firstly, the keystone distortion of the Dyson spectrometer is equal to 12 μm (1 pixel approximately), which is too high for a hyperspectral imager. Indeed, the maximum acceptable Keystone distortion is usually equal to a fraction of a pixel [8]. Secondly, the available space to implement the filter and camera is equal to 10 mm which is very small. We can thus expect that the assembly and alignment activities will be difficult for this spectrometer.

Table 7. TSC-1 Spectrometer Assembly trade-off summary.

Design	Advantage	Drawback
Dyson Spectrometer	Simple optical elements >Easy to manufacture, cost-effective solution. Concave grating >Easy to manufacture and control.	Small volume available to accommodate filter, slit and detector >Increases AIT and AIV complexity and risk. High Keystone distortion Detector located close to Dyson lens >Increase the level of ghost image irradiance.
Offner Spectrometer	Better image quality and negligible distortion Design comprising one mirror and one grating only >Eases assembly and integration test and verification activities (AIT & AIV)	Convex blazed grating >Difficult and expensive to manufacture

The Offner spectrometer presents a better theoretical image quality over the fully specified spectral domain and FOV. The theoretical keystone distortion is equal to 0.8 μm that is negligible when compared to the size of a pixel. Furthermore, the Offner provides sufficient space around the grating and the mirror to ease the assembly and the alignment. The only drawback is the shape of the grating, which is convex. However, we are confident that the state-of-art manufacturing methods using single-point diamond turning will be able to provide affordable convex gratings with performance compliant with the specifications. We thus decided to select the Offner spectrometer for the TSC-1 hyperspectral imager.

4. TSC-1 Payload Optical Design and Theoretical Performance

4.1. Optical Design and Theoretical Performance

To integrate the spectrometer with the front telescope, a flat-folding mirror is introduced under the FT-M1 with an angle of 10 degrees with respect to FT-M1 to fold the beam path and decrease the volume of the system as shown in Figure 10 left-panel. The light from the observing scene is incident on the FT-M1 and reflected toward FT-M2. The beam is reflected by FT-M2 toward the folding mirror before passing through the slit and entering the spectrometer. The beam from the slit is incident on SP-M1 and reflected toward the convex grating. The beam is diffracted by the grating and reflected back to the SP-M1. Finally, the spectrum is focused by SP-M1 onto the detector. The volume of the optical system is equal to $450 \times 400 \times 250$ mm^3.
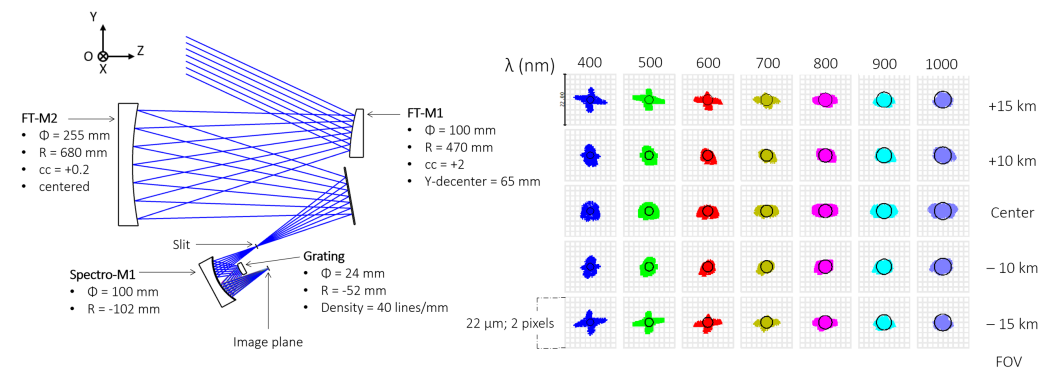

Figure 10. TSC-1 payload optical design, the list lies along the x axis (**left**-panel) and the spot diagram of the theoretical system (**right**-panel).

The spot diagrams of the theoretical system are represented in Figure 10-right panel. The maximum spot radius is equal to 3.7 μm meaning that the image is well contained within 2×2 pixels over the full specified FOV and spectral band.

The modulation transfer function (MTF) is the modulus of the optical transfer function. It describes the way the contrasts are transmitted by the optical system, from the object to the image [11]. The MTF at center FOV and λ = 700 nm is presented in Figure 11 for both tangential and the sagittal directions, which correspond to the spectral and the spatial directions respectively. We notice that the MTF at the Nyquist frequency (fn = 45 cycles/mm) is equal to 0.84 in the tangential direction and equal to 0.66 in the sagittal direction. That is much higher than the specified MTF that should be higher than 0.3 at the Nyquist frequency, thus showing that the system is fully compliant with this specification with margins.

The smile and keystone distortion maps are presented in Figure 12. The maximum smile distortion is equal to −24.8 μm at the edge of the FOV that is fully induced by the Front Telescope as discussed in Section 2.1. This requires the implementation of a curved slit on the focal plane of the Front Telescope. However, the smile distortion can be corrected by using image processing. It is important to mention that the smile distortion is invariant with respect to the wavelength. The maximum keystone distortion is reached at the edge of the FOV and λ = 1000 nm. This maximum, Keystone distortion is equal to 0.4 μm, which corresponds to less than 4% of the pixel, which is considered to be acceptable.
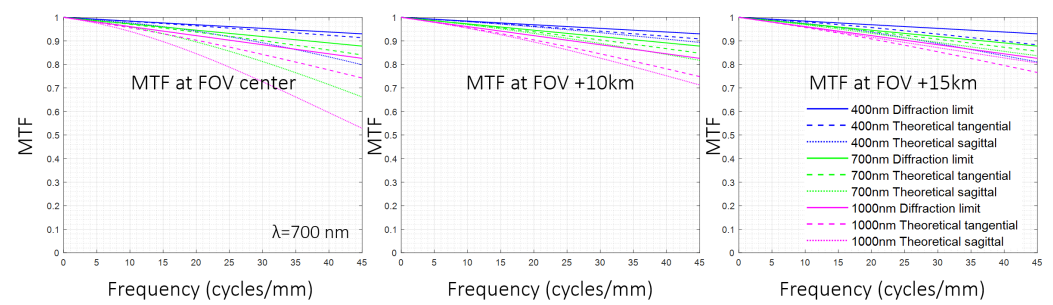
Figure 11. Modulation Transfer Function of the theoretical system at the FOV center, +10 km and +15 km and at λ = 400 nm, 700 nm and 1000 nm, for both the tangential plane (spectral direction) and the sagittal plane (spatial direction). The frequency varies between 0 cycles/mm and 45 cycles/mm (Nyquist frequency).
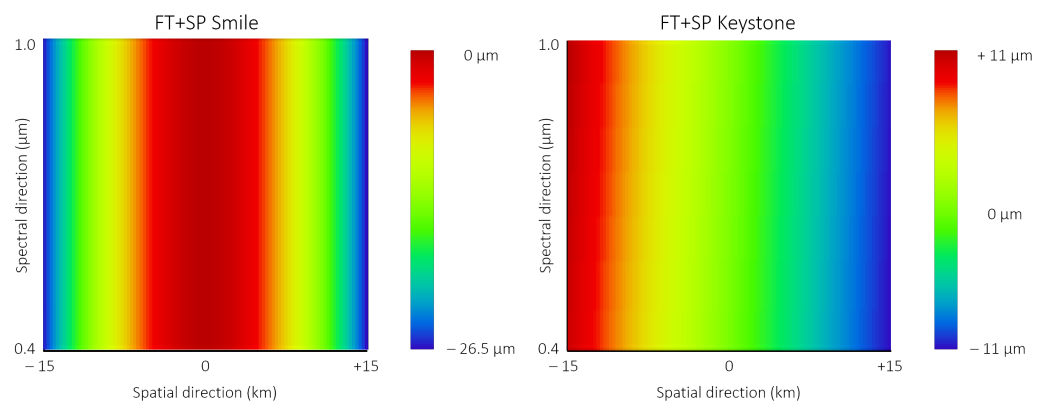

Figure 12. Theoretical smile (**left**-panel) and keystone (**right**-panel) distortion of TSC-1 optical payload.

It is important to mention that we also have been working on estimating the mechanical and thermal impacts on the optical system. The displacement of the optical components due to zero gravity effect and thermal expansion are estimated and are used to be the assumptions for the tolerancing analysis in Section 6. The results of the mechanical simulation will be presented in future dedicated communication.

4.2. Baffle Design, Windows, Filters and Coating Assumptions

The TSC-1 optical payload comprises two baffles located in front of FT-1 and in front of the spectrometer entrance silt. The Front Telescope baffle comprises four vanes, whose positions and dimensions (given in Table 8) have been calculated using the method proposed by Breault [16] to restrict the level of light coming from the Earth and incident on FT-M1 support. The spectrometer baffle comprises two vanes with parameters listed in Table 8. These parameters have been optimized by using the same method [16] to reject the residual level of straylight induced by the scattering on the payload structure and the mirror mounts. We identified through dedicated starlight analyses of the critical areas, which are both illuminated by Earth and seen by the detector. We found that only small fractions of FT-M2 and FM supports are illuminated during the observations and seen by the detector. We thus concluded that the payload is well protected from the straylight induced by the scattering of the light coming from Earth by the payload structure and that commercially available space-qualified black-coating such as Acktar [17] should be sufficient to reach an acceptable level of straylight. We decided to focus this work on the critical design parts and the performance. We decided not to include the results related to the identification of the critical areas in this paper.

Table 8. Entrance baffle and telescope focal plane baffle parameters.

Baffle Parameter		Value (mm)
Entrance Baffle	1st Vane External/Internal dimension	$140 \times 120/110 \times 78$
	2nd Vane External/Internal dimension	$140 \times 120/109 \times 78$
	3rd Vane External/Internal dimension	$140 \times 120/105 \times 78$
	4th Vane External/Internal dimension	$140 \times 120/98 \times 78$
	Distance between 1st vane–2nd vane	70.3
	Distance between 2nd vane–3rd vane	75.4
	Distance between 3rd vane–4th vane	80.6
Telescope focal plane baffle	1st Vane External/Internal dimension	$50 \times 50/27.3 \times 18$
	2nd Vane External/Internal dimension	$42.4 \times 42.4/175.5 \times 7$
	Distance between 1st vane–2nd vane	30
	Distance between 2nd vane—Slit	20

The optical components that induce the ghost images are all located in the spectrometer assembly represented in Figure 13. That includes the order sorting filter, the detector window and the detector surface. The order sorting filter is a glass plate of 2 mm thickness and located at a distance equal to 10 mm in front of the detector window.
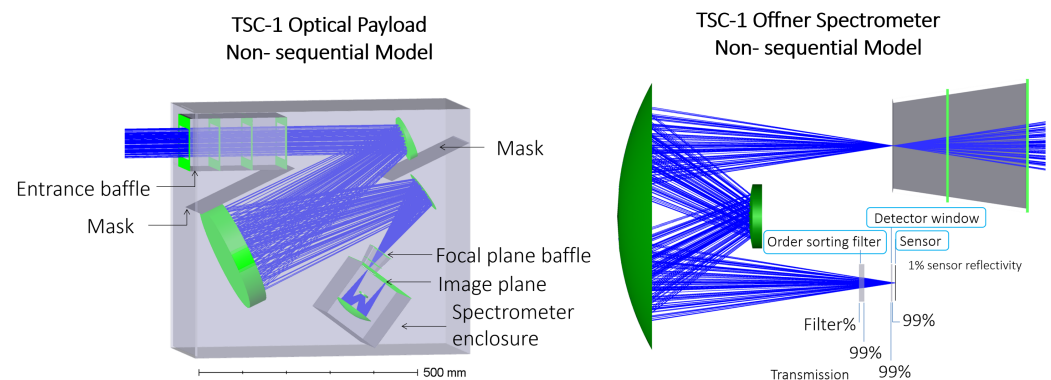

Figure 13. TSC-1 optical payload Non-Sequential Model developed under ZEMAX OpticStudio (**left**-panel) and close view on the model of the Offner Spectrometer assembly used to calculate the straylight induced by the ghost images (**right**-panel).

We assume that the order sorting filter that will be used in TSC-1 is similar to the order sorting filter of delta company [18]. In particular, the front face will be coated with a coating, whose transmission is equal to 98%. We assume that the back face of the order sorting filter is coated with an anti-reflective coating of transmission equal to 99% over the full TSC-1 spectral band. The detector window is made of a glass plate of thickness equal to 0.55 mm and located at a distance equal to 0.55 mm from the sensor chip. We assume that this window is coated with an anti-reflective coating on both faces with a reflectivity equal to 1% over the full specified spectral band. The ghost image caused by this setup will be discussed in Section 5.

5. Spatial and Spectral Responses and Contamination Level Comparing with Ghost Signal

In this section, we aim at estimating and comparing the contamination level to the adjacent pixels due to the theoretical responses and the contamination level due to the ghost image. The theoretical spatial and spectral responses are deduced by the convolution process between PSF provided by Zemax and the geometrical image of the target. On the other hand, the ghost image irradiance was already estimated by using the assumptions in Section 4.2.

5.1. Instrument Response Considering the Aberrations and the Diffraction

We estimated the theoretical response of the instrument over the specified FOV and spectral domain by calculating the irradiance incident on the detector while observing a ground-based square target of a length equal to 60 m. The geometrical image of this object thus covers a square area of length equal to two pixels on the detector. By applying the Nyquist criteria, we deduce that this target is the smallest target that can be resolved by TSC-1.

Firstly, we selected the FOV sample called FOV1, which is in the direction FOV = −15 km, and we selected the wavelength $\lambda 1$ = 400 nm. We extracted the theoretical Point Spread Function PSF (FOV1, $\lambda 1$) using Zemax OpticStudio. This PSF (FOV1, λ) was sampled over support of length equal to 38 μm with a sample step equal to 0.148 μm. That corresponds to 256 samples over the PSF at the wavelength equal to 400 nm. Secondly, we assumed that PSF (FOV1, $\lambda 1$) was invariant over the considered area of width equal to 110 × 110 μm², and we performed the convolution between PSF (FOV1, $\lambda 1$) and the geometrical image of the target by using the MATLAB software. Thirdly, we normalized the irradiance distribution by the maximum value. Fourthly, we resampled the irradiance distribution over a grid of size still equal to 110 × 110 μm², but of steps equal to 11 μm (same as pixel size) in both directions. The results correspond to the target image that would be provided by the TSC-1 optical payload in the theoretical case for the FOV1 and the wavelength $\lambda 1$, including the effect of the diffraction and the optical aberrations as represented in Figure 14. Finally, we repeated the operation for the FOV = 0 km, +10 km and +15 km and for the wavelength λ = 550 nm, 700 nm, 850 nm and 1000 nm.
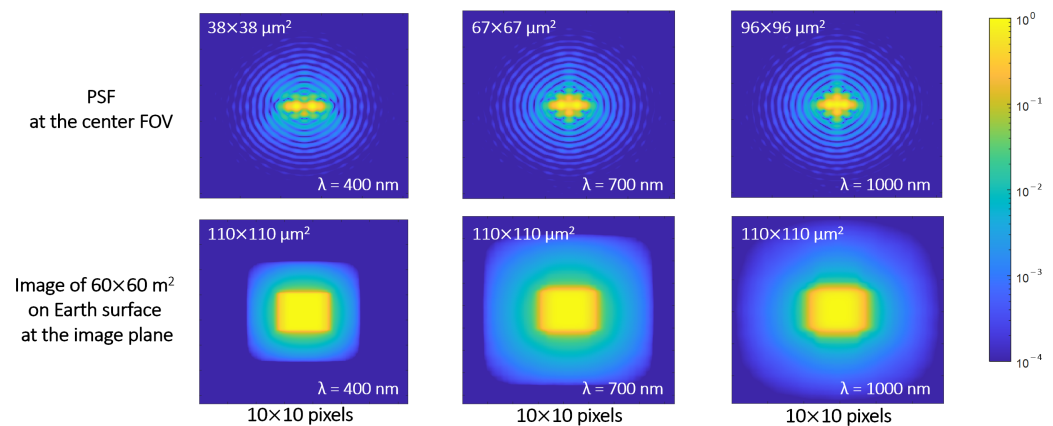

Figure 14. (**Top**-panel): on-axis normalized PSF at λ = 400 nm, 700 nm and 1000 nm and at FOV center provided by TSC-1 optical payload ZEMAX OpticStudio theoretical model. (**Bottom**-panel): result of the convolution between the geometrical image of a square target of on-ground size equal to 60 × 60 m² and the instrument PSF.

The orange curves of Figure 15 represent the cross-section across the spatial direction of the theoretical normalized irradiance distribution. This is for a target located on the FOV center and at wavelengths equal to 400 nm, 550 nm, 700 nm, 850 nm and 1000 nm. We notice that the aberrations and the diffraction induce a halo that surrounds the geometrical image of the target and that will induce contamination of the adjacent pixels. As expected, the level of the halo increases with the wavelength due to the diffraction effect and is maximum at λ = 1000 nm.

At the wavelength equal to 400 nm, the irradiance decreases to a level close to 10^{-3} at a distance equal to 22 μm from the target center to less than 10^{-5} at a distance higher than 33 μm. At the wavelength equal to 1 μm, the irradiance is equal to 10^{-2} at a distance equal to 22 μm, close to 10^{-3} at a distance equal to 33 μm and still higher than 10^{-4} at a distance equal to 44 μm.
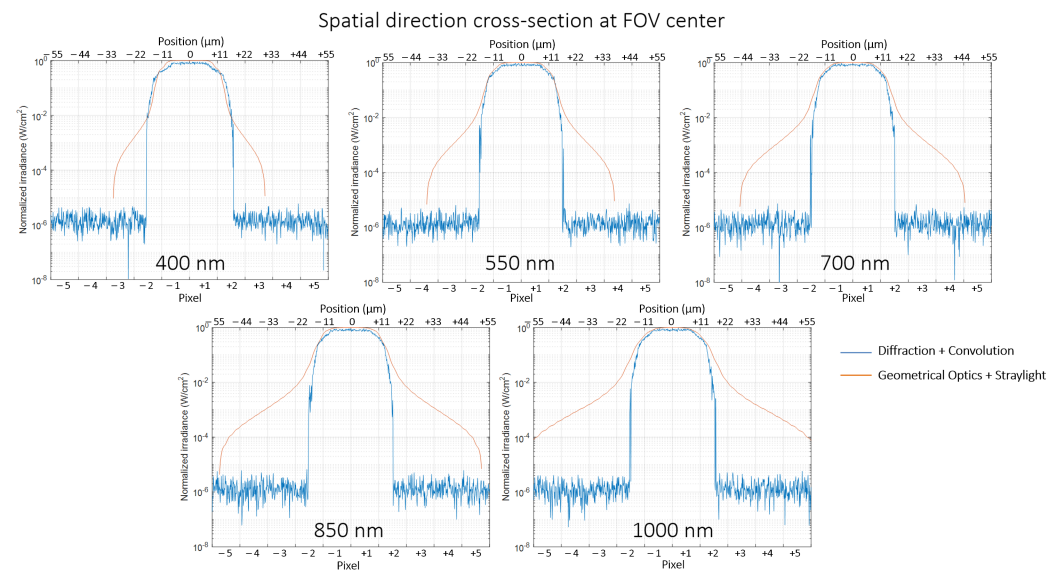
Figure 15. Relative irradiance cross-section at FOV center along spatial direction due to the diffraction (**orange curve**) and due to the straylight induced by the spurious reflections on the filters and the detector window (**blue curve**). The horizontal axis corresponds to the pixel. The vertical axis corresponds to the irradiance normalized by the maximum value reached on the pixels located on the geometrical image of the target.

The spatial response is larger for the longer wavelength according to the diffraction law. The irradiance level of the wavelength longer than 850 nm at a distance equal to 55 μm from the target center is equal to 10^{-4}. It is important to mention that we verified that similar results were obtained along the spectral direction and at the FOV values equal to -15 km and $+15$ km. We thus concluded that the FOV direction does not significantly impact the irradiance distribution of the image of the target considered for this study.

5.2. Straylight Background Irradiance

We estimated the level of the straylight due to the ghost image. We compare this contamination level with the level of the aberrations and the diffraction. This calculation was done by using the OpticStudio non-sequential model of TSC-1 represented in Figure 13 and the assumptions in Section 4.2. We used a square source of 60×60 m² on-ground emitting a beam that fully covers the TSC-1 optical payload entrance pupil. We launched 10^7 rays and calculated the irradiance incident of the detector with a minimum relative flux equal to 10^{-8} W/cm².

The blue curves in Figure 15 correspond to the irradiance calculated on the detector across the spatial direction. It is important to mention that these results include only the effects of the optical aberrations but do not include the effect of the diffraction.

At a distance smaller than 15 μm from the target center and at $\lambda = 400$ nm, 550 nm and 700 nm, we notice that the level of irradiance due to the ghost images is similar to the level of the irradiance induced by the aberrations and the diffraction. At $\lambda = 400$ nm, we even notice that the level of the straylight is slightly higher than the level of the diffraction.

We notice that at a distance higher than 15 μm, the level of the background induced by the ghost images is always one million times fainter than the signal measured by the central pixels located on the paraxial image of the source. We also notice that the level of the irradiance of the halo induced by the spurious reflections is always lower that the irradiance of the halo induced by the aberrations and the diffraction by a few orders of magnitudes and at every wavelength across the specified spectral domain. It is important to mention that we obtained similar results along the spectral direction and at the FOV equal to -15 km and $+15$ km.

5.3. Contamination between Adjacent Pixels

In this section, we estimate the level of the irradiance coming from an on-axis source that contaminates the nearby pixels. The source is square, located on-ground along the optical axis and of length equal to 60 m. In the ideal case (geometrical optics without optical aberrations), this irradiance induced by this target on the detector should be fully concentrated on a group of four pixels. In reality, the optical aberrations, the diffraction and the straylight induce halos around the geometrical image as discussed in the previous section. The consequence is that the pixels not located on the geometrical image of the on-axis source also receive a fraction of the energy emitted by the on-axis source. For this reason, we consider that the energy coming from the on-axis source "contaminates" the adjacent pixels.

We call I_{Max} the irradiance incident on the group of 2 × 2 pixels located on the geometrical image of the source and set the contamination of these pixels equal to 0%. The irradiance incident on the adjacent pixels is called I_{Pix}. We defined the contamination level as ContLevel = I_{Pix}/I_{Max}. Figure 16 presents the contamination due to the on-axis source induced by the aberrations and the diffraction and due to the straylight induced by the internal multiple reflections. The area of 10 × 10 pixels around the center of the image of each wavelength is shown. The pixel coordinate that will be used to discuss in this section is defined by pixel (row, column).
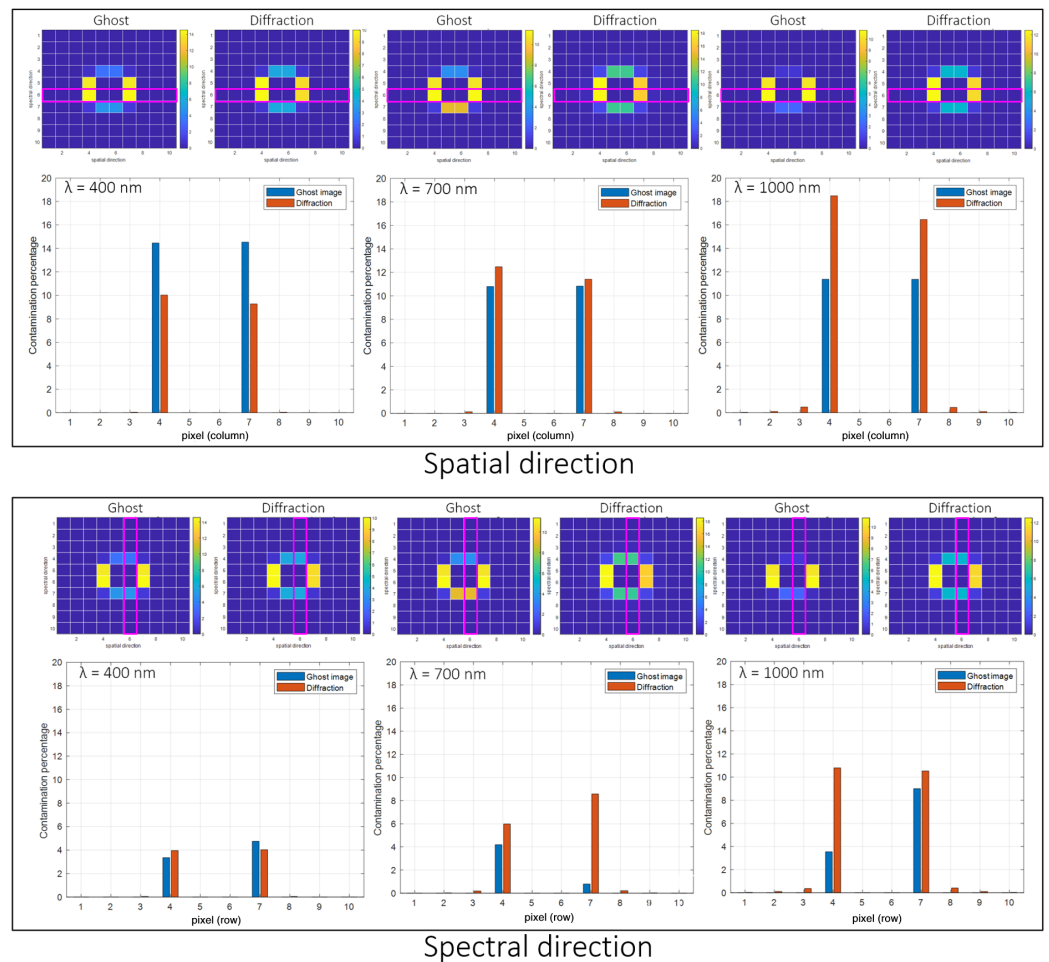

Spatial direction

Spectral direction

Figure 16. Contamination level due to ghost image (blue) and aberrations and diffraction (red) in the spatial (**Top**-panel) and spectral (**Bottom**-panel) directions, where x and y axis of the 2D contamination maps are labeled as spatial direction and spectral direction respectively. The pixel coordinate is defined by pixel (row, column).

Along the spatial direction, we notice that, at $\lambda = 400$ nm, the contamination on pixel (6, 4) and pixel (6, 7) in Figure 16 located in the immediate vicinity of the central pixels and due to the ghost image is equal to 14%. This level of contamination is thus higher than the contamination due to the aberrations and the diffraction close to 10% on the same pixels. The contamination of the other pixels is much smaller than 1% and is thus fully negligible. At $\lambda = 700$ nm, the contamination induced by the diffraction and the straylight on the pixel (6, 4) and pixel (6, 7) in Figure 16 reaches a similar level between 11% and 12%. At $\lambda = 1000$ nm, the contamination induced by the aberrations and the diffraction is much higher and is between 18% and 16% on pixel (6, 4) and pixel (6, 7) respectively.

Across the spectral axis, we notice a similar tendency but with smaller levels of contamination. Indeed, at $\lambda = 400$ nm, 700 nm, and 1000 nm, the maximum contamination levels are equal to 5%, 9% and 11% only. The reason for the small contamination level is that the shape of the PSFs expands in the spatial direction rather than the spectral direction due to the aberrations of the optical system as shown in Figure 14 Top-panel.

The contamination level due to the ghost image in spatial direction at the lower wavelength is higher than the contamination level due to the aberrations and the diffraction. The contamination in the spatial direction from both sources is at the same level at $\lambda = 700$ nm. Then, the contamination level due to the aberrations and the diffraction starts to dominate at a longer wavelength. On the other hand, the contamination in the spectral direction from both sources is at the same level at $\lambda = 400$ nm. Then, the contamination due to the aberrations and the diffraction starts to dominate at a longer wavelength. We conclude that the ghost signal is dominant in the short wavelength. However, the longer the wavelength is, the higher the contamination due to the aberrations and diffraction in both spatial and spectral directions.

6. Tolerancing and Performance Budget

6.1. Overall Method

The tolerancing analysis aims at estimating the impact of the manufacturing and the in-orbit misalignment errors on the performance of the optical system at the end of life. In this section, we calculate the "End-Of-Life" spot radius (R_{EOL}) using the following relation:

$$R_{\text{EOL}} = R_{\text{Theo}} + \Delta R_{\text{EOL}}, \tag{1}$$

where R_{Theo} is the theoretical RMS spot radius of the perfect system. For example, the theoretical RMS spot radius at the FOV center and at $\lambda = 700$ nm is $R_{\text{Theo, 700 nm}} = 1.5$ μm. ΔR_{EOL} is the End-Of-Life RMS spot radius enlargement due to the errors on the optical surface quality and the misalignment described by the following relation:

$$\Delta R_{\text{EOL}} = \sqrt{\Delta R^2_{\text{Manu}} + \Delta R^2_{\text{Assem}} + \Delta R^2_{\text{stab}}}, \tag{2}$$

where ΔR_{Manu}, ΔR_{Assem} and ΔR_{stab} are the RMS spot radius enlargement due to the manufacturing errors, assembly errors and stability of the optical payload during the operational condition respectively.

6.2. Manufacturing Tolerancing Analysis

In this section, we estimate the variation of the image quality performance induced by the errors in manufacturing. We assume that the optical components are manufactured by OPTIMAX company with the precision level [19]. Therefore, the radius of curvature error shall be lower than ±0.1% and the irregularity of the surface shall be lower than 0.15 μm PTV. We use the positions and the orientations of FT-M2 and the detector as compensators to correct the aberrations that are induced by manufacturing errors. We assume that the FT-M2 position along the z-axis and tip/tilt can be adjusted by ±1 mm and ±1 degree. The detector position along the z-axis can be adjusted within an amplitude of ±1 mm without the possibility to tilt this detector. The manufacturing tolerancing cumulative probability is presented in Figure 17-blue curve. ΔR_{Manu} is the spot radius enlargement

due to the set of errors in the manufacturing process. We notice that ΔR_{Manu} is lower than 0.5 µm in the realistic case at cumulative probability equal to 95% and lower than 1 µm in the worst case. That represents less than 10% of the pixel size and is thus negligible. We conclude that manufacturing errors will have a minor impact on image quality.
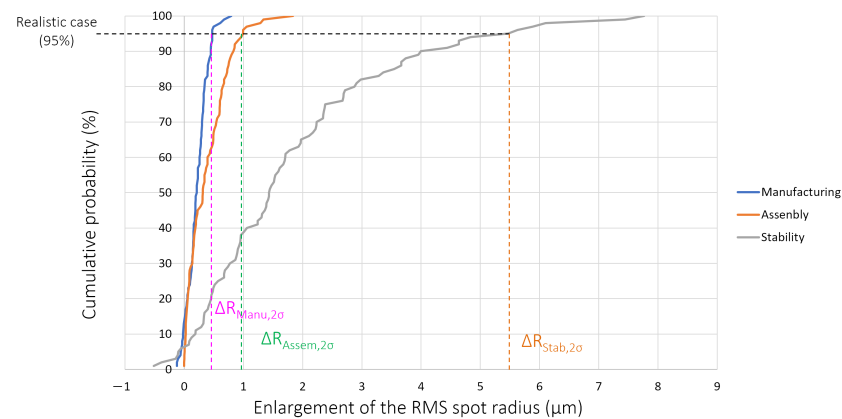

Figure 17. Cumulative probability curves of RMS spot radius enlargement at FOV center and λ = 700 nm for the Manufacturing, Assembly and Stability tolerancing analyses.

6.3. Assembly Tolerancing Analysis

We performed assembly tolerancing analysis to estimate the variation of the spot radius enlargement induced by the assembly and alignment activities ΔR_{Assem}. We assume that the misalignment of each optical component shall be lower than 30 µm in both positions along x, y, z and at the edge of the component (tip/tilt) according to preliminary finite element analysis results. The only compensator is the position of the detector which has been optimized to decrease the overall spot radius over the full specified FOV and the spectral domain. The amplitude of the compensator has been equal to ± 1 mm along the z-axis which is considered realistic.

The assembly tolerancing results are presented in Figure 17—orange curve. ΔR_{Assem} is the spot radius enlargement due to the set of errors in the assembly process. We notice that ΔR_{Assem} is smaller than 1 µm in the realistic case and smaller than 2 µm in the worst case. That corresponds to only 20% of the pixel size. We thus conclude that the residual alignment errors induced by the optical alignment will have a negligible impact on the image quality.

6.4. Stability Tolerancing Analysis

This tolerancing analysis aims at estimating the enlargement of the spot image induced by the mechanical stability and thermal effect during the operational condition ΔR_{stab}. That includes the combination of both the zero-gravity and the thermo-elastic effects. We assume that the maximum displacement of the optical surfaces and the detector due to these effects will be equal to 20 µm. We also assume that the displacement of the spectrometer assembly with respect to the Front Telescope will be equal to 10 µm. It is important to mention that the TSC-1 payload will be fully passive without any mechanism to optimize the focus during the observation. For this reason, the stability tolerancing analysis does not include any kind of compensator.

The stability tolerancing results are presented in Figure 17—gray curve. ΔR_{stab} is the spot radius enlargement due to the set of errors in the stability process. We notice that ΔR_{stab} is equal to 5.5 µm in the realistic case and equal to 7.8 µm in the worst case. That corresponds to 70% of the size of the pixel that is significant. We can thus already conclude that the stability of the system will be the most important contributor to the image quality at the end of life.

6.5. Performance Budget

Table 9 presents summarizes the ΔR values obtained after performing the Manufacturing, Assembly and stability tolerancing analyses and the value of the ΔR_{EOL} calculated by using Equation (2). We notice that ΔR_{EOL} varies from 2.3 μm in the typical case to 5.5 μm in the realistic case, to 8 μm in the worst case. As discussed in the previous sections, stability is the most dominant contributor to spot radius enlargement.

Table 9. Calculation of ΔR_{EOL} for each individual contributor in the typical, realistic and worst case at λ = 700 nm.

Spot Radius Enlargement	Typical Case (68%)	Realistic Case (95%)	Worst Case
ΔR_{Manu} (μm RMS)	0.3	0.5	0.8
ΔR_{Assem} (μm RMS)	0.5	1.0	1.8
ΔR_{Stab} (μm RMS)	2.2	5.5	7.8
ΔR_{EOL} (μm RMS)	**2.3**	**5.5**	**8.0**

Table 10 represents the values of R_{Theo}, ΔR_{EOL} and R_{EOL} estimated by applying Equation (1). We notice that the End-Of-Life spot radius will vary from 4 μm in the typical case to 7 μm in the realistic case and to 9.5 μm in the worst case. We thus conclude that the end-of-life spot radius will be smaller than the pixel size with a margin equal to 2 μm that is considered acceptable.

Table 10. Theoretical and End-of-Life spot radius for the typical, realistic and Worst cases at λ = 700 nm.

Spot Radius Enlargement	Typical Case (68%)	Realistic Case (95%)	Worst Case
R_{Theo} (μm RMS)	1.5	1.5	1.5
ΔR_{EOL} (μm RMS)	2.3	5.5	8.0
R_{EOL} (μm RMS)	**3.8**	**7.1**	**9.5**

7. Radiometric Performances

7.1. Method and Assumptions

The objective of this section is to establish the SNR budget of the TSC-1 optical payload and to calculate the aperture number of the payload to comply with the specifications. The payload is specified to provide the SNR higher than 150 over the full specified spectral domain for an incident radiance L = 70 W/m^2/sr/μm.

The flux collected by the optical payload is:

$$F = L \times \Delta\lambda \times T \times GE, \tag{3}$$

where $\Delta\lambda$ is the spectral sampling that is collected by a pixel. T is the optical payload throughput which includes the reflectivity of each mirror, the grating diffraction efficiency and the transmittance of both the anti-reflective coatings and the order-sorting filter. GE is the geometrical extend of the instrument that depends on the system aperture number ($F\#$) and the area of one pixel (A_{R}):

$$GE = \pi \frac{1}{4F\#^2} A_{\text{R}} \tag{4}$$

The signal corresponds to the number of electrons obtained within the integration time δt:

$$S = \frac{F}{hc/\lambda} \times QE \times \delta t, \tag{5}$$

where QE is the Quantum Efficiency of the detector.

The noise includes the dark noise (N_D), the readout noise (N_R) and the shot noise (N_S). The dark and the readout noises are provided by the detector manufacturer company. The shot noise corresponds to the photon noise induced by the receiving flux from the observing scene: $N_S = \sqrt{S}$. The noise is calculated by computing the quadratic summation of the variances of the different sources of noise:

$$N = \sqrt{N^2{}_D + N^2{}_R + N^2{}_S} \tag{6}$$

We thus conclude that the expression of the *SNR* is:

$$SNR = \frac{S}{\sqrt{N^2{}_D + N^2{}_R + N^2{}_S}} \tag{7}$$

Firstly, we calculate the integration time δt_1 that corresponds to an on-ground shift equal to $x = 30$ m. We found that $\delta t_1 = 4.37$ ms by applying the following equations:

$$\delta t = \frac{x}{v_{surface}}, \tag{8}$$

$$v_{surface} = \frac{v_{orbit} \times R_E}{R_{orbit}}, \tag{9}$$

$$v_{orbit} = \sqrt{\frac{GM_E}{R_{orbit}}}, \tag{10}$$

where x is the on-ground shift along the track. In our case, $x = 30$ m which corresponds to the value of the specified *GSD*. $v_{surface}$ is the pass-by velocity of the satellite on the ground. v_{orbit} is the velocity of the satellite in the orbit at altitude H. R_E is the radius of the Earth. R_{orbit} is the satellite orbiting radius from the center of the Earth $R_{orbit} = R_E + H$. G is the gravitational constant. M_E is the mass of the Earth.

Secondly, we assume that we can increase the integration time up to $\delta t_2 = 13.11$ ms by keeping an on-ground shift equal to 30 m. We use the forward motion compensation technique to slow down the push-broom velocity of the satellite by a factor of 3. It is done by using the agility of the three-axis stabilized platform to stabilize the line of the sign of the payload.

Table 11 summarizes the assumptions made to calculate the radiometric performance. We assume that the detector is the CMOSIS CMV-4000 detector [20]. The fill factor of the sensor is equal to 42% without microlenses. The dark noise of each individual pixel is equal to 125 e/s at 25 °C. The readout noise is equal to 13 e/pix. The pixel size after 2 × 2 binning is equal to 11 μm. The aperture number of the optical system is equal to 3. The spectral sampling is equal to 5 nm/pixel. The optical payload throughput at $\lambda = 700$ nm is equal to 54.2% which includes a throughput of the front telescope and of the spectrometer equal to 85.7% and 63.2% respectively.

Table 11. Radiometric budget assumptions.

Parameter	Assumption
Dark and Readout noise	125 e/s/pix @ 25 °C and 13 e/pix
Pixel size	11 μm
Spectral radiance	70 W/m^2/sr/μm
Spectral sampling, *GSD*	5 nm, 30 m
Flight altitude	630 km
Optical payload throughput	$T = 0.54$ at $\lambda = 700$ nm
Aperture number	F/3
Integration time	$\delta t_1 = 4.37$ ms and $\delta t_2 = 13.11$ ms

7.2. Results and Conclusions

Figure 18-left-panel represents the variation of the SNR with respect to the wavelength. We notice that in the case of an integration time δt_1 = 4.37 ms, SNR is higher than 100 the spectral range 430 nm to 840 nm only and non-compliant (NC) otherwise. The maximum SNR is equal to 160 at λ = 620 nm. In case δt_2 of 13.11 ms, SNR is higher than 100 over the spectral range 400 nm to 910 nm and NC otherwise. That is considered acceptable due to the unavoidable drop of QE at wavelengths higher than 900 nm. The maximum SNR is equal to 270 at λ = 620 nm.
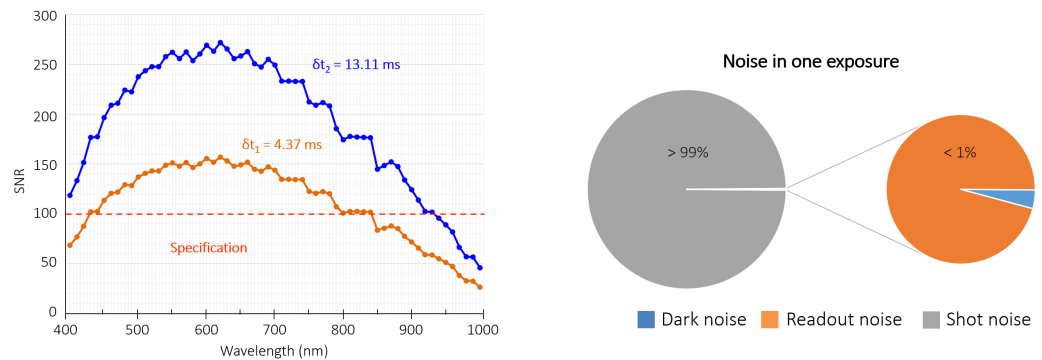
Figure 18. TSC-1 Signal-To-Noise Ratio performance over full specified spectral domain (**left**-panel) and Contributors to SNR performance at the wavelength λ = 700 nm in the case δt_2 = 13.11 ms (**right**-panel).

Figure 18-right-panel represents the relative contribution of the different sources of noise at the integration time δt_2 = 13.11 ms. We notice that the most important noise contributor is the shot noise which corresponds to more than 99% of all noises.

8. Conclusions

In this paper, we presented the trade-off analysis we performed to select the design of the front telescope and the spectrometer. We described the optical design that comprises one front telescope and an Offner spectrometer. We presented the preliminary mechanical design and the concept of the passive thermal control system that will be used to stabilize the temperature in operational conditions.

We estimated that the theoretical image quality of the payload is close to the diffraction limit over the full specified Field of View. This is the theoretical case (no misalignment) and the realistic case. The smile distortion of the front telescope makes the necessary use of a curved slit. On the other hand, the smile and the keystone distortions of the Offner spectrometer are fully negligible. The performance summary of the TSC-1 Hyperspectral imager is presented in Table 12.

We calculated the spatial and spectral responses of the instrument and estimated the contamination of the adjacent pixels. We found that at λ = 400 nm the maximum level of contamination was equal to 15% of the signal from the observing scene and was induced by the ghost images while at λ = 1000 nm, the contamination was close to 20% of the signal from the observing scene and was induced by the diffraction.

Finally, we showed that the SNR should be higher than 100 over the spectral range from 400 nm to 910 nm with a maximum value equal to 270 at λ = 620 nm when the forward motion compensation technique is used.

The next steps will aim at preparing the TSC-1 optical payload preliminary design review that will be held in mid-2023. Firstly, we will optimize the mechanical design by implementing some light-weighting in the optical bench and FT-M2 mirror design. Secondly, we will optimize TSC-1 thermal control to reach negligible deformations induced by the gravity-released and thermo-elastic effects. Thirdly, we will define the calibration method and implement the calibration devices in the payload. Finally, we will update the

performance budget to justify that the payload will provide performance compliant with the specifications in operational conditions.

Table 12. TSC-1 Hyperspectral imager performance budget summary.

Attribute	Performance
- Selected FT RMS spot radius at FOV center	<2.2 μm
- Selected FT distortions	Maximum 24 μm at the edge of FOV
- Selected Spectrometer (Offner) RMS spot radius at λ = 700 nm and FOV center	1 μm
- Selected Spectrometer (Offner) distortions	Smile: <1 μm Keystone: <1 μm
- TSC-1 Hyperspectral Imager RMS spot radius at λ = 700 nm and FOV center	<1.5 μm
- Theoretical system distortion	Maximum smile: 24.8 μm @ the edge of FOV Maximum keystone: <1 μm
- EOL spot radius at λ = 700 nm and FOV center	Typical: 3.8 μm
	Realistic: 7.1 μm Worst: 9.5 μm
- Adjacent pixel contamination by diffraction at λ = 700 nm and FOV center	Spatial direction: 13% of the signal Spectral direction: 11% of the signal
- Adjacent pixel contamination by straylight at λ = 700 nm and FOV center	Spatial direction: 9% of the signal Spectral direction: 5% of the signal
- SNR > 150 for δt_1 = 4.37 ms	[430 nm, 840 nm]
- SNR > 150 for δt_2 = 13.11 ms	[400 nm, 910 nm]

References

1. Buisset, C.; Deboos, A.; Lepine, T.; Poshyachinda, S.; Soonthornthum, B. Design and performance estimate of a focal reducer for the 2.3 m Thai National Telescope. *Opt. Express* **2016**, *24*, 1416–1430. [CrossRef] [PubMed]
2. Buisset, C.; Prasit, A.; Lepine, T.; Poshyachinda, S.; Soonthornthum, B.; Deboos, A. Opto-mechanical design and development status of an all spherical five lenses Focal Reducer for the 2.3 m Thai National Telescope. *Proc. SPIE* **2016**, *9906*, 99062F.

3. Prasit, A.; Buisset, C.; Lepine, T.; Ridsdill-Smith, M.; Chakpor, A.; Leckngam, A.; Thummasorn, G.; Ngernsujja, S.; Inpan, A.; Kaewsamoet, P.; et al. Installation, alignment method, and preliminary test results of the Thai National Telescope focal reducer. *Proc. SPIE* **2019**, *11116*, 111161A.
4. Lhospice, E.; Buisset, C.; Jones, H.R.; Martin, W.E.; Errmann, R.; Sithajan, S.; Boonsri, C.; Choochalerm, P.; Anglada-Escude, G.; Campbell, D.; et al. EXOhSPEC folded design optimization and performance estimation. *Proc. SPIE* **2019**, *11117*, 111170Z.
5. Paenoi, J.; Buisset, C.; Suwansukho, K.; Sirichote, W.; Choochalerm, P.; Aukkaravittayapun, S.; Thummasorn, G.; Ngernsujja, S.; Inpun, A.; Kaewsamoeta, P.; et al. The Design and On-sky Results of the Prototype of a Low-Resolution Spectrograph for the Thai National Telescope. *Curr. Appl. Sci. Technol.* **2020**, *20*, 1.
6. Drinkwater, N.R.; Rebhan, H. *Sentinel-3: Mission Requirements Document*, 2nd ed.; Mission Document; ESA: Paris, France, 2007.
7. Sang, B.; Schubert, J.; Kaiser, S.; Mogulsky, V.; Neumann, C.; Forster, K.P.; Hofer, S.; Stuffler, T.; Kaufmann, H.; Muller, A.; et al. The EnMAP hyperspectral imaging spectrometer: Instrument concept, calibration, and technologies. *Proc. SPIE* **2008**, *7086*, 708605.
8. Qian, S. *Hyperspectral Satellites and System Design*, 1st ed.; CRC Press: Boca Raton, FL, USA, 2020.
9. Optical Design Software. Available online: https://www.zemax.com/pages/opticstudio (accessed on 1 August 2022).
10. Wanajaroen, W.; Lepine, T.; Buisset, C.; Castelnau, M.; Costes, V.; Wannawichian, S.; Poshyachinda, S.; Soonthornthuma, B. Hyperspectral spectro-imager survey for state of art concept identification. *Proc. SPIE* **2021**, *11852*, 1185268.
11. Gross, H. *Handbook of Optical Systems Volume 4*, 1st ed.; WILEY-VCH Verlag GmbH & Co. KGaA: Weinheim, Germany, 2008.
12. Warren, D.W.; Gutierrez, D.J.; Hall, J.L.; Keim, E.R. Dyson spectrometers for infrared earth remote sensing. *Proc. SPIE* **2008**, *7082*, 70820R.
13. Van Gorp, B.; Mouroulis, P.; Wilson, D.W.; Green, R.O. Design of the Compact Wide Swath Imaging Spectrometer (CWIS). *Proc. SPIE* **2014**, *9222*, 92220C.
14. Van Gorp, B.; Mouroulis, P.; Wilson, D.W.; Green, R.O.; Rodriguez, J.I.; Liggett, E.; Thompson, D.R. Compact Wide swath Imaging Spectrometer (CWIS): Alignment and laboratory calibration. *Proc. SPIE* **2016**, *9976*, 997605.
15. Reimers, J.; Bauer, A.; Thompson, K.P.; Rolland, J.P. Freeform spectrometer enabling increased compactness. *Light Sci. Appl.* **2017**, *6*, e17026. [CrossRef] [PubMed]
16. Bass, M. *Handbook of Optics: Fundamentals, Techniques, and Design*, 2nd ed.; McGraw-Hill: New York, NY, USA, 1995.
17. Acktar World Leader in Black Coating. Available online: https://www.acktar.com (accessed on 1 August 2022).
18. Continuously Variable Filters (a.k.a. Linear Variable Filters)/CVSWP 395 nm–815 nm. Available online: https://www.deltaopticalthinfilm.com/product/cvswp-395-nm-815-nm (accessed on 1 August 2022).
19. Manufacturing Tolerance Chart. Available online: https://www.optimaxsi.com/optical-manufacturing-tolerance-chart (accessed on 1 August 2022).
20. AMS CMV-4000 CMOS Sensor Datasheet. Available online: https://ams.com/documents/20143/36005/CMV4000_DS000728_4-00.pdf (accessed on 1 August 2022).